Applied Physics A (2021) 127:831
https://doi.org/10.1007/s00339-021-04974-z

Applied Physics A
Materials Science & Processing

Interplay between cation distribution and magnetic properties for $CoAl_xFe_{2-x}O_4$ $0.0 \leq x \leq 0.7$ nanoparticles

Ebtesam E. Ateia[1] · K. K. Meleka[1] · F. Z. Ghobrial[1]

Received: 19 September 2021 / Accepted: 29 September 2021

Abstract
The relationship between cationic distribution, bond angle, bond length with magnetic properties of $CoFe_{2-x}Al_xO_4$ ($0 \leq x \leq 1$) nano-ferrite is demonstrated. The magnetic properties of spinel nano-ferrites have been examined using a vibrating sample magnetometer. The crystal structure was calculated using an X-ray diffractometer and ratified via high-resolution transmission electron microscopy. Substitution of Al content (x) in cobalt ferrite caused a reduction in particle size, lattice parameter, and magnetic properties. The saturation magnetization changes with increasing Al content due to the effect of cation distribution in tetrahedral and octahedral sites and due to a change in ferrimagnetic structure. The existence of the strong dipolar interactions and/or exchange coupling is established via the appearance of double peaks in switching field distribution. The obtained data ratify that the substitution of Al content in the cobalt system is a powerful tool for tuning the magnetic properties of the investigated samples. This substitution decreases the magnetic energy loss and the switching field distribution. Consequently, the studied samples are recommended to be used in transformer cores and high-density recording. The strong correlation between cation distribution, bond angle, bond length, and the magnetic properties of the studied samples is the main advantages of the present work as compared to the literature reported on Co-Al nano-ferrite.

Keywords Switching field · Magnetic properties · Doped nano-ferrite

1 Introduction

The spinel nano-ferrites have novelty and fascinating technological applications due to their attractive physical properties [1–6]. The nanosized-cobalt ferrite has enormous applications in all technological fields depending on the exclusive microstructure and cation distribution [7–12].

Cobalt ferrite is a partially inverse spinel structure with space group Fd3m. It represents as $(Co_x^{2+}Fe_{1-x}^{3+})$ $[Co_{1-x}^{2+}Fe_{1-x}^{3+}]$ O_4, where ( ) and [] brackets designate the tetrahedral (A) and octahedral sites, respectively. [7]. The magnetic properties of cobalt spinel nano-ferrite can be adapted by adding Al cations. This addition changes the microstructure properties such as crystal size, effective bond lengths, lattice constant, crystalline density, and cations distribution between A and B-sites [13–17]. The most crucial parameters that affect the expected physical properties of the resulting doped cobalt ferrite nanoparticle are the synthetization process as well as the content of the doped cation [18, 19].

The citrate-gel auto-combustion method was used for the synthesizing of the investigated samples due to its low cost, short time of production, purity, and homogeneity of the final product, narrow size distribution, and controlled stoichiometry [20].

The ferrite nanoparticles containing cobalt, aluminum, and chromium were studied by Mane et al. [21]. They concluded that aluminum ion substitution has a noticeable effect on softening and regulating the magnetic properties of hard cobalt ferrites. Hanh et al. [22] prepared cobalt ferrite nanoparticles by the forced hydrolysis method. They found that the addition of trivalent ions like Al^{3+}, instead of Fe^{3+} ion into Co, Zn, the system greatly influences both their electrical and magnetic properties [23].

In the present work, the $CoAl_xFe_{2-x}O_4$ nanoparticles were synthesized using the auto-combustion technique and characterized samples by numerous procedures. The structural and magnetic properties of the system are testified. One of the challenges faced in this study is to focus on the relationship between the cation distribution, bond angle,

✉ Ebtesam E. Ateia
drebtesam2000@yahoo.com

[1] Physics Department, Faculty of Science, Cairo University, Cairo, Egypt

Published online: 13 October 2021

and the magnetic properties of the studied samples. The switching field distribution for Al^{3+} doped cobalt ferrite nanoparticles examined in this report can be considered as one of the few studies done in this field.

2 Experimental work

$CoAl_xFe_{2-x}O_4$ ($x = 0.0, 0.3, 0.5, 0.7$) samples were manufactured by the citrate-gel auto-combustion method using stoichiometric amount of high purity (99%, Fisher chemicals) $Co(NO_3)_2\ 6H_2O$, $Al(NO_3)_3$, and $Fe(NO_3)_3$. The citric acid was used to enhance the homogeneous mixing, and the deionized water is used as a solvent. All powders are calcined at 600 °C for 4 h with a heating rate of 4 °C/min as shown in Fig. 1.

The structure and crystallite sizes were tested by X-ray diffraction (XRD) pattern using Diano Corporation target Cu-K_α ($\lambda = 1.5418$ A°). The nano-particles average sizes were estimated using Scherer's relationship [24]. The morphology of the samples was studied by high-resolution transmission electron microscopy (HRTEM) and, field emission scanning electron microscope (FESEM) attached with EDAX unit (energy-dispersive X-ray analysis). Room-temperature magnetic hysteresis of the nano-ferrite samples was measured by maximum field 20kOe using vibrating sample magnetometer (VSM) model, Lake shore 7410.

Fig. 1 Flow chart for the synthetic scheme

3 Results and discussion

3.1 Structural analyses

3.1.1 XRD analysis

Figure 2 shows the X-ray diffraction pattern for $CoAl_xFe_{2-x}O_4$ ($0 \le x \le 0.7$). All samples are formed in a single-phase without any impurity as shown from the figure. The XRD pattern exhibits broad diffraction corresponding to the cubic spinel crystalline single phase (ICDD card no. (00–001-1121)) indexed to (220), (311), (222), (400), (422), (511), and (440) planes, belonging to Fd3m space group [18].

The calculated lattice parameter varies from 8.412 to 8.304 A° depending on the Al content [25]. This decrease of the lattice parameter is elucidated by many issues. The first issue is the doping cation (Al) that has a smaller ionic radius (0.535) compared to that of Fe (0.645). The second is the possible redistribution of the cations between the tetrahedral (A) and octahedral (B) sites, which will be followed by significant changes in the magnetic properties. Another issue is a fraction of cations occupying the B site and forcing Al^{3+} ions into the A site against their chemical preferences [26].

On the other side, Debye–Scherrer's equation [24] is utilized to calculate the crystallite size of the samples (D). The size is estimated from the broadening of the respective high intensity (311) peak. As the Al content x is increased the diffraction peaks became broader. This broadening with Al^{3+} content points to the decrease of characteristic size. The results are shown in Table 1. A similar trend was reported for $NiFe_{2-x}Al_xO_4$ system [27, 28].

The movement of O^{2-} ion due to the substitution of cation at "A" site is characterized by the oxygen parameter "u". The

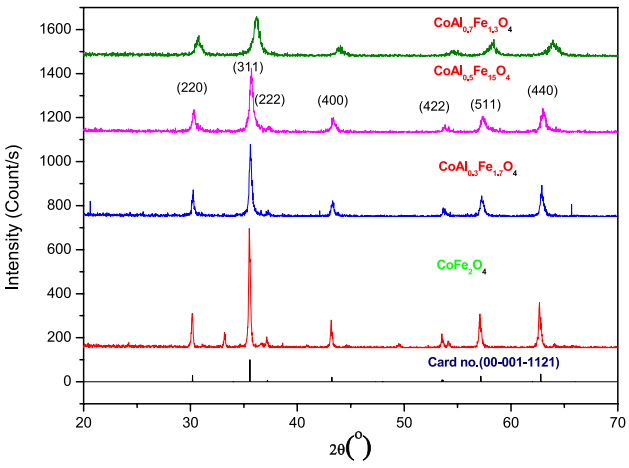

Fig.2 The X-ray diffraction pattern for $CoAL_xFe_{2-x}O_4$ ($x = 0.0, 0.3, 0.5, 0.7$)

Table 1 Crystallite size (D), theoretical (atheo) and experimental (aexp) lattice parameters, X-ray density (Dx), the radii of the tetrahedral (rA) and octahedral (rB) sites and oxygen parameter (u) of $CoAl_xFe_{2-x}O_4$

Cation distribution	D (nm)	aexp (Å)	atheo (Å)	Dx (gm/cm^3)	rA (Å)	rB (Å)	u (Å)
$(Fe^{+3})_{IV}\left\|Co^{+2}Fe^{+3}\right\|_{VI}O_4$	52.2	8.412	8.412	5.235	0.49	0.695	0.378
$(Co^{+2}_{0.35}Fe^{+3}_{0.635}Al^{+3}_{0.015})_{IV}\left\|Co^{+2}_{0.65}Al^{+3}_{0.285}Fe^{+3}_{1.065}\right\|_{VI}O_4$	39.6	8.371	8.370	5.118	0.52	0.662	0.381
$(Co^{+2}_{0.4}Fe^{+3}_{0.565}Al^{+3}_{0.035})_{IV}\left\|Co^{+2}_{0.6}Al^{+3}_{0.465}Fe^{+3}_{0.935}\right\|_{VI}O_4$	23.57	8.349	8.341	5.037	0.522	0.65	0.382
$(Co^{+2}_{0.1}Fe^{+3}_{0.835}Al^{+3}_{0.065})_{IV}\left\|Co^{+2}_{0.9}Fe^{+3}_{0.515}Al^{+3}_{0.635}\right\|_{VI}$	14.8	8.304	8.309	4.973	0.502	0.671	0.381

"u" parameter for the ideal spinel has a value nearly equals to 0.375, whereas for the actual spinel lattice u > 0.375. It is observed that the calculated value of u is greater than 0.375 and increases with increasing Al content [29]. This means that the distance between A–O ions increases and that between B–O ions decreases [30] causing a decrease in A–A interaction, and an increase in B–B interaction as will be discussed.

For the spinel system, the theoretical lattice constant (a_{th}) can be detected via knowing the ionic radii of the ions at the B site (r_B), and the A site (r_A). These calculations are based on the distribution of cations as illustrated in the following relation [31]:

$$r_A = \mathbf{x_{Co}} r\left(Co^{2+}\right) + x_{Fe} r\left(Fe^{3+}\right) + x_{Al} r\left(Al^{3+}\right)$$

$$r_B = 1/2\left[x_{Co} r\left(Co^{2+}\right) + x_{Fe} r\left(Fe^{3+}\right) + x_{Al} r\left(Al^{3+}\right)\right] \quad (1)$$

The ionic radii; r(Co^{2+}), r(Fe^{3+}), r(Al^{+3}) are taken according to Shannon [24]. x_{Co}, x_{Fe} and, x_{Al} are the ion concentration of Co^{2+}, Fe^{3+}, and Al^{3+} on different sites taking into account the corresponding cation distribution. The (a_{th}) is determined using the equation [20]:

$$a_{th} = \frac{8}{3\sqrt{3}} r_{A-O} + \frac{8}{3} r_{B-O} \quad (2)$$

where r_o is the radius of the oxygen ion (1.38 A°). The calculated values agree well with that experimental data. The X-ray density can be calculated as reported in the previous work [32]. The decrease of the theoretical density with increasing Al^{3+} content can be attributed to the smaller molecular weight of Al^{+3} (26.982 gm/mol) compared to that of iron (55.845 gm/mol) [9].

3.1.2 Microstructural features

The homogeneity of the investigated samples can be ratified via the high-resolution transmission electron micrographs (HRTEM), d spacing, and the selected area electron diffraction patterns (SAED). Figure 3a–f shows the typical HRTEM for $CoFe_2O_4$, and $CoAl_{0.3}Fe_{1.7}O_4$ samples. It is detected that the particle size distribution is nearly homogeneous and the particles are agglomerated in nanometric size. The observed agglomeration is due to the magnetic interactions between nanoparticles [33]. The morphology evaluation shows a tendency to decrease the particle size with the substitution of Al in the system. This means that the presence of Al inhibits crystal growth. The reduction in the size is due to two issues the first is the size mismatch between Fe^{3+} and Al^{3+} ions, while the second is the flexibility of Al substitution into the available sites during particle growth, thus limiting the nucleation process [34]. The observed pores in the samples may be due to the release of excess amounts of gases during the combustion method [35]. The SAED shape consists of concentric rings with spots over the rings. This characteristic designates that the samples have good nano-crystalline in nature [36]. The rings with a dotted pattern in SAED ratify the widespread size distribution of ferrite nano-particles. The patterns provide the d-spacing consistent with those obtained from XRD studies. The lattice fringes of the core, as detected from the HRTEM images, also approve the single crystalline nature of the studied samples.

Figure 3g–i represents the energy-dispersive X-ray (EDAX) spectrum for $CoAl_xFe_{2-x}O_4$ nano-particles (x=0.3 0.5, 0.0). The estimation of elements obtained from the spectrum through its weight and atomic percentages are illustrated in the inset of the figure. The elemental analysis attained from EDAX is in good agreement with the used materials during the preparation.

3.1.3 Surface topography using AFM

Atomic force microscopy is an excellent procedure to testify surface topography and texture of the different surfaces of the ferrite nanoparticles. Figure 4a–b shows the 3-D AFM micrographs of $CoFe_2O_4$, and $CoAl_{0.5}Fe_{1.5}O_4$. AFM images for all samples show that the surfaces have hillocks over the entire scanned region. The obtained particle size from AFM is larger compared to the XRD data [37].

Figure 4c–d represents the histograms of the root mean square roughness of the investigated sample which indicates the decrease of the roughness with increase Al^{+3} concentrations. This is due to the decrease in grain and crystal size by

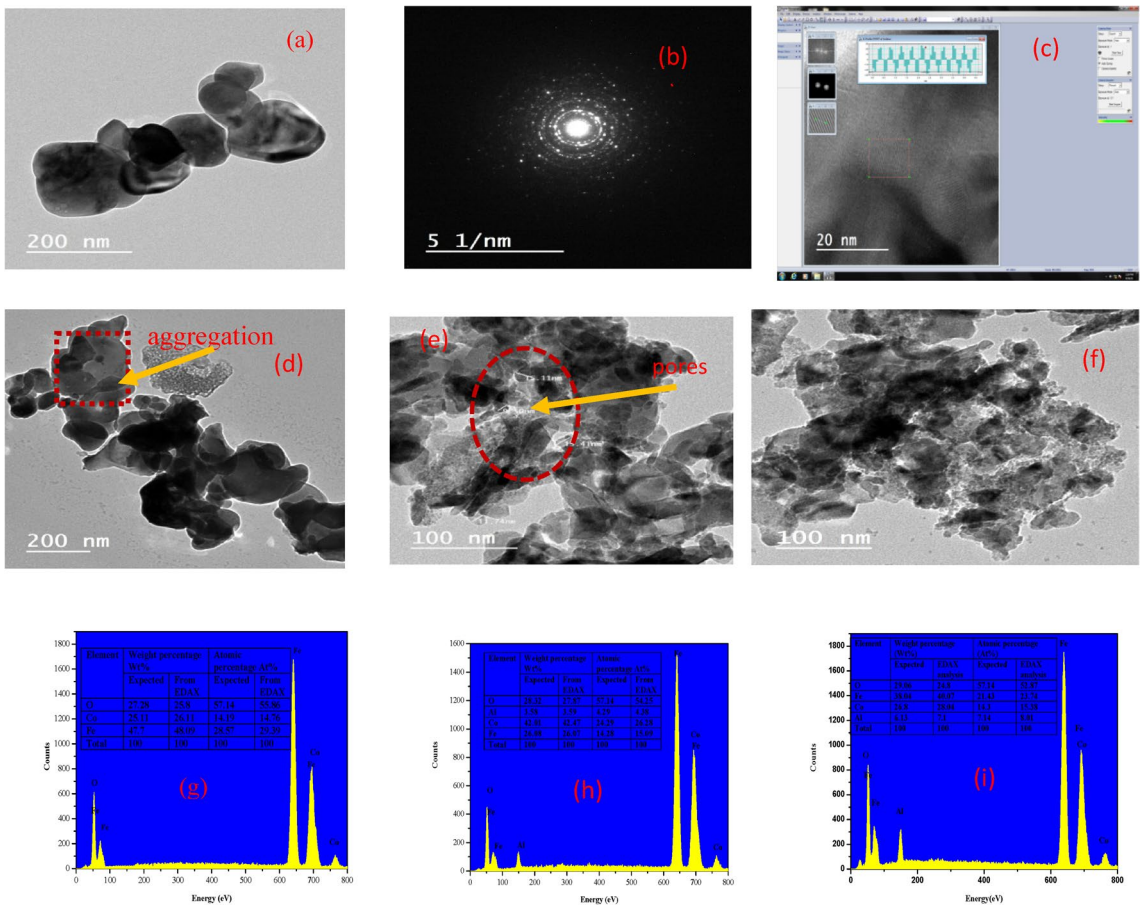

Fig. 3 **a–f** The HRTEM images, **g–i** the EDAX analysis for Co $Al_xFe_{2-x}O_4$; $0.0 \leq x \leq 0.7$

adding Al^{+3} ions and the large spreading of the nanoparticles over a larger surfaces area [38].

3.1.4 Thermal analysis

Thermo-gravimetric analysis (TGA) and differential scanning calorimetric (DSC) for $CoAl_{0.3}Fe_{0.7}O_4$ and $CoAl_{0.5}Fe_{1.5}O_4$ are shown in Fig. 4a–c.

$$0.3Al(NO_3)_3.9H_2O + Co(NO_3)_2.6H_2O + 1.7Fe(NO_3)_3.9H_2O + C_6H_8O_7.H_2O \rightarrow CoAl_{0.3}Fe_{1.7}O_4 + 4N_2 + 6CO_2 + 29H_2O + 5.5\ O_2$$

$$0.5Al(NO_3)_3.9H_2O + Co(NO_3)_2.6H_2O + 1.5Fe(NO_3)_3.9H_2O + C_6H_8O_7.H_2O \rightarrow CoAl_{0.5}Fe_{1.5}O_4 + 4N_2 + 6CO_2 + 29H_2O + 5.5\ O_2$$

As shown from the figure, the TGA traces exhibit three distinct weight loss steps. In the temperature range 30–150 °C, the weight loss is due to the dehydration process where an insignificant amount of adsorbed water is released from the wet chemically synthesized nano-ferrite samples. The further weight loss during 150–300 °C is correlated to the decomposition of nitrates, some organic residues that are left in the samples, and removal of OH ions. Finally, a steady change in weight is detected up to 1000 °C. The maximum losses for the investigated samples appear in the range of 300–800 °C. The typical nitrate-citrate auto-combustion reaction for the entire precursor can be presented as [39] (Fig. 5a–c)

The DSC graph for the $CoFe_2O_4$ sample shows a wide exothermic peak which designates the temperature range for crystal recovery, while the presence of the endothermic and exothermic peaks indicates phase and magnetic transition for $CoAl_{0.3}Fe_{1.7}O_4$ and $CoAl_{0.5}Fe_{1.5}O_4$. No weight

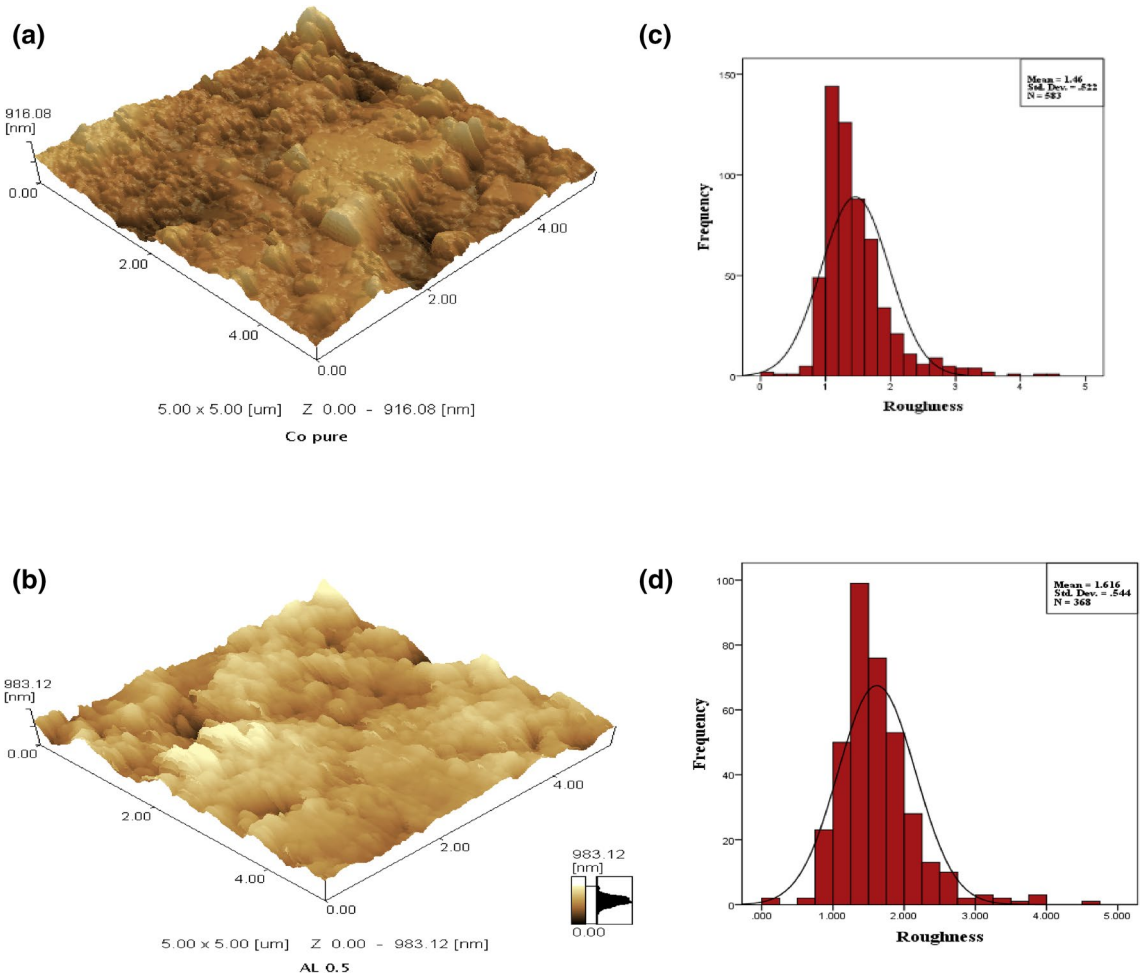

Fig. 4 **a–b** AFM image, **c–d** The roughness of the $CoFe_{2-x}Al_xO_4$; (x = 0.0, and 0.5) nano-ferrite sample

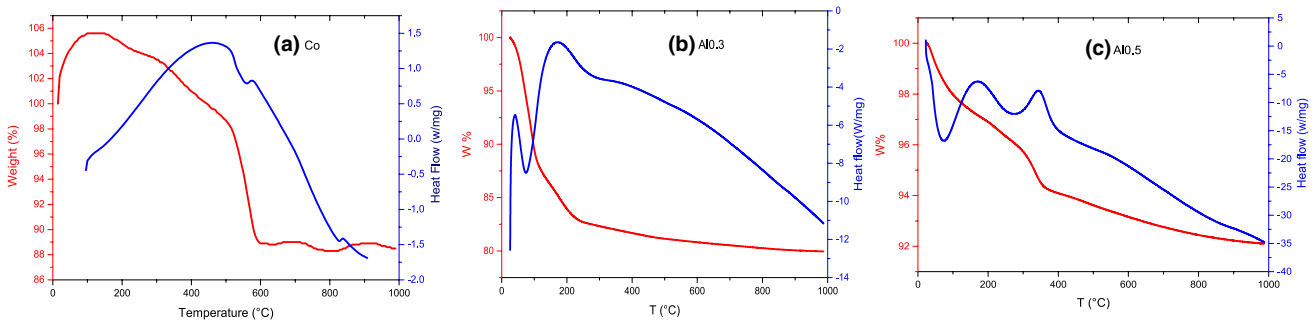

Fig. 5 **a–c** The TGA, and DSC for **a** Co and **b** $Al_{0.3}$ **c** $Al_{0.5}$

gain is observed for $CoAl_{0.3}Fe_{1.7}O_4$ and $CoAl_{0.5}Fe_{1.5}O_4$. On the other side, the observed weight gain for $CoFe_2O_4$ is due to the oxidation process [40].

Considering the DSC and TGA data of the investigated samples, a temperature of 600 °C is selected for sintering the sample to obtain the maximum crystalline phase.

3.2 Magnetic properties measurements

In general, the size and the shape of the hysteresis curve for ferromagnetic materials are of considerable importance. Figure 6a–b illustrates the magnetization versus external magnetic field (M–H) hysteresis loop and the

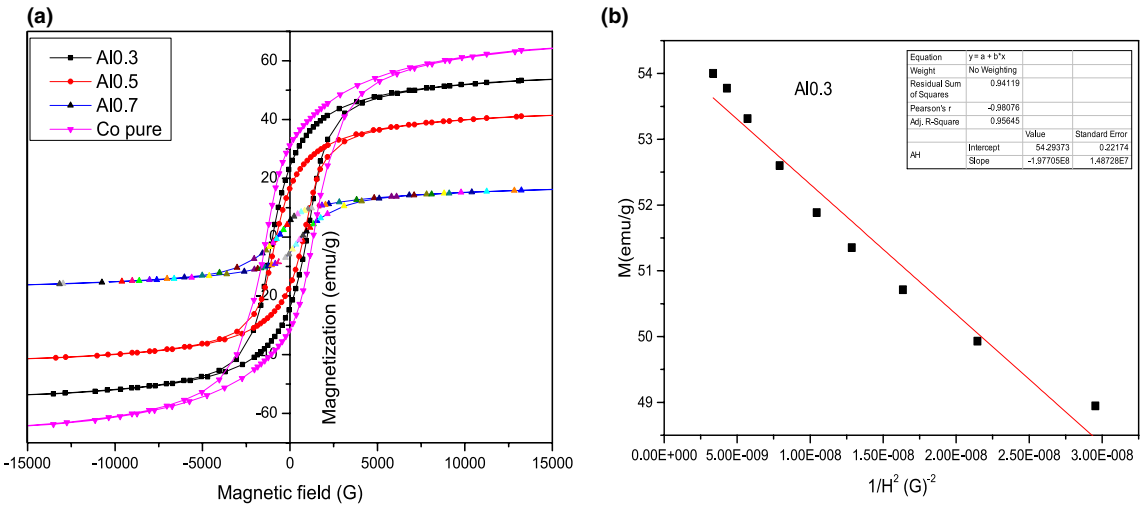

Fig. 6 **a** The hysteresis loops for $CoAl_xFe_{2-x}O_4$; $0.0 \le x \le 0.7$ nano-ferrite **b** fitting plot between *M* versus $1/H^2$

fitted Langevin curve. The experimental M versus H loop is determined with an external applied magnetic field ranging between −20 and +20 kOe. The saturation magnetization (*Ms*) value that corresponds to 20 kOe is 53.79 emu/g. The M_s of Co $Al_{0.3}Fe_{1.7}O_4$ nanoparticle also can be detected by an approximation of Stoner–Wohlfarth theory by extrapolating the plot of magnetization versus $1/H^2$ to approach zero [41, 42]. This theory is applied for non-interacting particles as confirm from squareness values in the Table. In this way, the M_s value is equal to 54.29 emu/g. Both the calculated and the experimental values agree well with each other. This conclusion ratifies that an applied field of ±20 kOe is appropriate to saturate the studied samples.

The properties such as saturation magnetization (M_s), remnant magnetization (M_r), coercivity (H_c), observed magnetic moments ($n_{\mu obs}$), calculated magnetic moments ($n_{\mu cal}$), the Yafet–Kittel angles (α_{Y-K}), and anisotropy constant (K) are illustrated in Table 2.

In general, the aluminum Al^{3+} as nonmagnetic ions are known to be 'B' sites preferable than less percentage of Al^{3+} ions occupy 'A' sites in the present system. The replacement of an Al^{3+} ion that has no magnetic moment (0 μB) instead of a Fe^{3+} ion (5 μB) will dilute the magnetization at the octahedral site and hence reduces the magnetic moment and accordingly the magnetization of the lattice. Consequently, the reduction in both magnetization and the area of the hysteresis loops will change the investigated system from hard to soft ferrite, accordingly, the $CoFe_{1-x}Co_xO_4$ is appropriate for high-frequency devices.

The anisotropy constant 'K' is estimated from the Stoner–Wohlfarth relation as follows [43]

$$K = \frac{H_C \times M_S}{0.98} \tag{3}$$

Non-collinearity (canting) of spins on the surface of the samples, as well as the decrease of spin–orbit coupling, is the main issue for the obtained data.

Table 2 illustrates the estimated magnetic parameters of $CoAl_xFe_{2-x}O_4$; $0 \le x \le 0.7$. The variation of coercivity with particle size is explained on the basis of the domain size of the particle and crystal anisotropy [44]. Also, it may be caused by lowering the anisotropy barrier in small particles

Table 2 Estimated remnant magnetization (M_r), saturation magnetization (M_s), squareness (M_r/M_s). Coercivity (H_c), Magnetic anisotropy (K), the magnetic moment of A and B sites, experimental magnetic moments, the Yafet–Kittel angles, and switching field distribution (SFD) of $CoAl_xFe_{2-x}O_4$; $0 \le x \le 0.7$

Sample	M_r emu/g	M_s emu/g	M_r/M_s	H_c (G)	K (G.emu)/g × 10^3	MA (μB)	MB (μB)	nB (calcu)	nB (exp) (μB)	αY-K	SFD
$CoFe_2O_4$	30.838	65.07	0.474	1486.4	98.74	5	8	3	2.73	14.93	1.68
$CoAl_{0.3}Fe_{1.7}O_4$	23.869	53.79	0.444	984.69	54.10	4.225	7.275	3.05	2.18	28.44	2.03
$CoAl_{0.5}Fe_{1.5}O_4$	16.604	41.68	0.398	778.57	33.12	4.025	6.475	2.45	1.64	28.97	2.38
$CoAl_{0.7}Fe_{1.3}O_4$	5.4711	16.58	0.33	677.25	11.46	4.475	5.275	0.8	0.64	14.15	3.69

and the small anisotropy density in the case of higher Al content [45].

The squareness (M_r/M_s) is the significant characteristic parameter for applications for ferro/ferrimagnetic materials. The compositional variation of the squareness is listed in the Table. The gradually decrease of M_r/M_s with Al content indicates the switching to the multidomain nature of the highly doped Al samples.

However, the magnetic parameters decrease with increasing Al content as shown in the Table. Similar behavior was reported for Al-substituted soft ferrites [46]. It is obvious from Table 2 that the values of n_{Bexp} are systematically lower compared to that calculated by the Neel model n_{Bcal}. This difference suggests a deviation from the perfect collinear structure of spins in the tetra and octahedral sites. Consequently, the system cannot be elucidated completely by the Neel model, but can be elucidated by Yafet and Kittel's model [47, 48]. The Yafet–Kittel angles (α_{Y-K}) describe the spin canting created by the dopants.

The values of α_{Y-K} have been calculated using the following formula [49]

$$\alpha_{YK} = \cos^{-1}\left(\frac{n_B + M_A}{M_B}\right) \tag{4}$$

where M_A, M_B are the magnetic moment of A and B sites, respectively, expressed in the units of Bohr magneton (μB). The magnetic moment of Co, Fe, and Al is 3 μB, 5 μB, and 0 μB, respectively [34]. The experimental magnetic moment is calculated as mentioned in the previous work [50], and tabulated in the Table.

The value of the α_{Y-K} angle is in the range 14.15–28.97°, which ratifies the existence of a triangular (canted) spin arrangement in $CoAl_xFe_{2-x}O_4$. This indicates that the randomness and frustration increase with increasing Al content and a significant departure from the Neel-type collinear magnetic order is detected [51]. Similar results have been reports for Cu-Mn and Mg-Zn ferrites [52, 53]. Initially, for $0 \le x < 0.7$ α_{YK} increases suggest triangular spin arrangements on the B site, results in the weakening of A-B interaction and strengthening B–B interaction.

The decrease of α_{YK} for samples with $x = 0.7$ implies a reduction of triangular spin arrangement on the B. Additionally, the increase in Al content ($x = 0.7$) leads to an increase of Fe migration from B-site to A-site and consequently increases the net magnetic moment of A site. Accordingly, an increase in the A–A interaction and a decrease in the B–B interaction are expected. Furthermore, information on magnetic interactions can also be obtained via bond angles as discussed below.

The types and the distribution of cations between A and B sites have a strong effect on the exchange interactions among them. In ferrites, there are three reasonable super exchange interactions as follows: A–A, B–B, and A–B interactions (Fig. 7) where the A-B interaction is much strongest one.

The strength of the A–B, B–B, and A–A interactions depends on both the bond lengths and bond angles between the cations and cation–anion. The strength of interaction varies directly with bond angle and inversely with bond length for the $CoFe_{2-x}$ Al_xO_4; ($0 \le x \le 0.7$) spinel nano-ferrites.

The bond lengths are tabulated in Table 3, while the bond angles (θ_1, θ_2, θ_3, θ_4, and θ_5) between the cations and cation–anion are estimated using the following relations and tabulated in Table 4 [54, 55]

Table 3 The estimated bond distances for $CoAl_{0.3}Fe_{1.7}O_4$

Me–O	Me–Me
$p = a\left(\frac{5}{8} - u\right) = 2.042$	$b = \sqrt{2}\left(\frac{a}{4}\right) = 2.69$
$q = a\sqrt{3}\left(u - \frac{1}{4}\right) = 1.901$	$c = \sqrt{11}\left(\frac{a}{8}\right) = 3.47$
$r = a\sqrt{11}\left(u - \frac{1}{4}\right) = 3.64$	$d = \sqrt{3}\left(\frac{a}{4}\right) = 3.625$
$s = a\sqrt{3}\left(\frac{u}{3} + \frac{1}{8}\right) = 3.65$	$e = \sqrt{3}\left(\frac{3a}{8}\right) = 5.44$
	$f = \sqrt{6}\left(\frac{a}{4}\right) = 5.126$

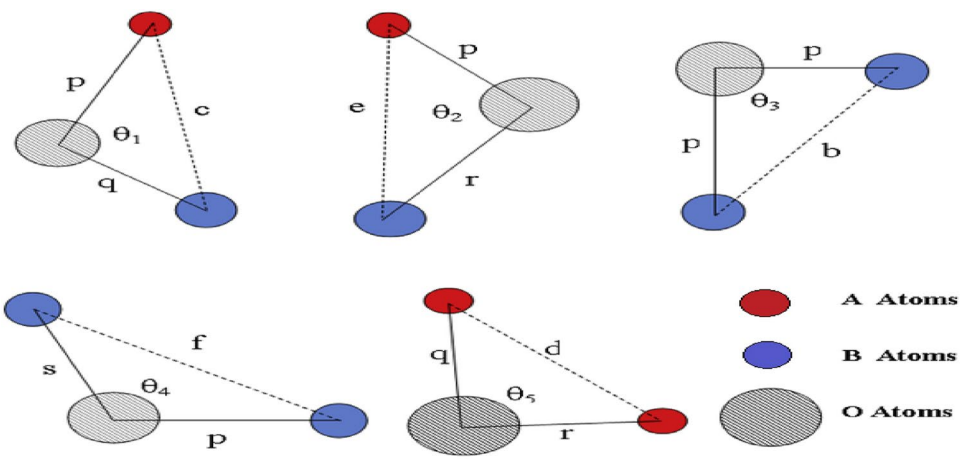

Fig. 7 Schematic configuration of the ion pairs in spinel ferrite with favorable distances and angles for effective magnetic interactions

Table 4 The estimated bond angles for $CoAl_{0.3}Fe_{1.7}O_4$

Samples	θ_1°	θ_2°	θ_3°	θ_4°	θ_5°	αY-K
$CoFe_2O_4$	124.3	149.5	91.4	125.6	77.1	14.93
$CoFe_{1.7}Al_{0.3}O_4$	123.3	145	95.93	125.9	74.4	28.44
$CoFe_{1.5}Al_{0.5}O_4$	123.1	144.3	93.11	126.7	74	28.97
$CoFe_{1.3}Al_{0.7}O_4$	123.4	145.2	92.81	125.9	74.6	14.15

$$\theta_1 = \cos^{-1}\left(\frac{p^2+q^2-c^2}{2pq}\right),\ \theta_2 = \cos^{-1}\left(\frac{p^2+r^2-e^2}{2pr}\right),$$
$$\theta_3 = \cos^{-1}\left(\frac{p^2-b^2}{2p^2}\right),\ \theta_4 = \cos^{-1}\left(\frac{p^2+s^2-f^2}{2ps}\right),$$
$$\theta_5 = \cos^{-1}\left(\frac{r^2+q^2-d^2}{2rq}\right) \quad (5)$$

In the present case, the estimated bond angles for the $CoFe_{2-x}Al_xO_4$ ($0 \le x < 0.7$) indicate that θ_1, θ_2, and θ_5 decrease, while θ_3 and θ_4 nearly increase with increasing Al^{2+} ion content. This can be attributed to the cationic rearrangement due to Al-doping as confirmed from the previous discussion. The increase in θ_3 and θ_4 indicates a strengthening of B–B interactions, while θ_1, θ_2, and θ_5 decrease, which is indicative of weakening A–B and A–A interactions.

The correlation between bond angle and canting angle αYK is detected. Table 4 shows the bond angle and the α_{YK}, essentially depending on Al content. Consequently, the fluctuation of the strengthening of B–B and the weakening of the A–B interaction is detected.

Figure 8 shows the switching field distribution field SFD value for the $CoAl_xFe_{2-x}O_4$; $0.0 \le 0.7$ as a function of coercivity. Its value is calculated from the following equation as the ratio of the half-width of the peak in the $\partial M/\partial H$ and coercivity

$$SFD = \frac{\Delta H}{Hc} \quad (6)$$

Double peaks are detected for all studied samples as shown in the figure. Generally, the observed peaks ratify the competition between exchange coupling and strong dipolar interactions. Adjusting the dipolar field energy and the exchange coupling energy to a value of the same order leads to a double peak derivative. The first peak comes from the saturation field and occurs before reaching zero-field [56]. Therefore, for the investigated sample, the dipolar interactions are more effective, which implies a strong reduction of the inter bump exchange coupling in our bump array.

From the above arguments, it is concluded that the small SFD value of the investigated sample is due to an intrinsic magnetic nature such as uniformity of substitution and crystallinity as confirmed from XRD data.

4 Conclusion

The citrate auto-combustion technique was successfully used to obtain $CoFe_{2-x}Al_xO_4$ ferrite nanoparticles. The crystallite sizes of the studied samples are in the range of 52–14 nm depended on Al ion concentration. The M_s decreases with increasing Al content and can be correlated to the weakening of the super exchange interaction between A-site and B-site. The reduction in the magnetization and the hysteresis loops will change the investigated system from hard to soft ferrite; accordingly, the $CoFe_{1-x}Co_xO_4$ is appropriate for high-frequency devices.

Distinct advantage and uniqueness of the manuscript as compared to the previous literature (8, 41, 47, 54, 56) lies in the strong correlation between cation distribution, bond

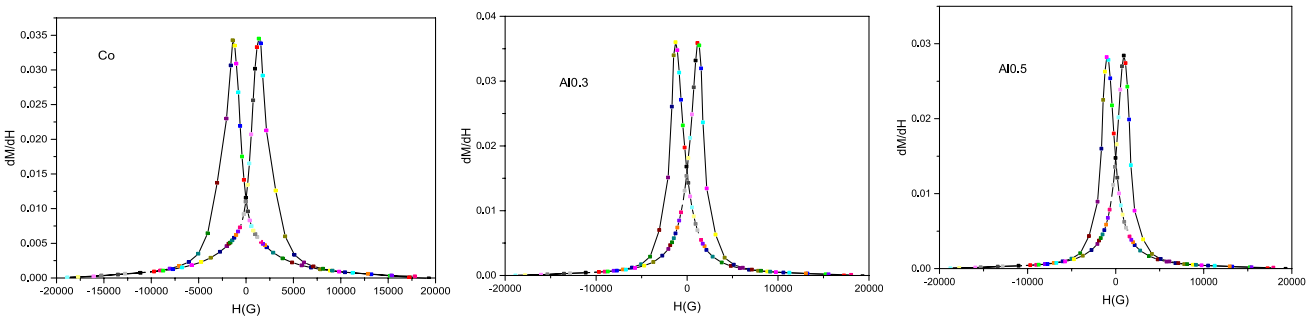

Fig. 8 **a**–**d** Switching field distribution for $CoAl_xFe_{2-x}O_4$ with $x = 0.0$, 0.3, and 0.5 at room temperature

angle, bond length, canting angle α_{YK} and the magnetic properties of the $CoAl_xFe_{2-x}O_4$ $0.0 \le x \le 0.7$ nanoparticles.

The Yafet and Kittel's model is more appropriate to elucidate the investigated system compared to the Neel model.

Acknowledgements I would like to express my gratitude and appreciation to Asmaa A. H. El-Bassuony, and Dalia. N. Ghaffar, physics department, Faculty of Science, Cairo University, for their moral support.

Authors' contribution *Ebtesam E. Ateia* contributed to conceptualization, methodology, validation, formal analysis, investigation, resources, data curation, writing–original draft preparation, writing–review & editing, visualization, and supervision. *K. K. Meleka* contributed to material preparation, data collection and analysis, optimum selection of material parameters, methodology, validation and visualization, review and editing. *F. Z. Ghobrial* contributed to conceptualization, investigation, and review and editing.

Funding This research did not receive any specific grant from funding agencies in the public, commercial, or not-for-profit sectors.

Declarations

Conflict of interest The authors declare that they have no known competing financial interests or personal relationships that could have appeared to influence the work reported in this paper.

References

1. B. Purnama, A. Khoiriah, S. Suhatyana, Structural and magnetic properties of aluminum-substituted cobalt ferrite nanoparticles synthesized by the Co-precipitation Route. J. Magn. **23**(1), 106–111 (2018)
2. Z. Zlozarevic, C. Jovolevic, A. Milutnovic, M.J. Romecvic, Z. Romcevice, Preparation and characterization of nanoferrite. Acta Phys. Pol. A **21**, 682 (2012)
3. D.-M. Wei, J.-B. Li, Y.-J. Chen, Cation distribution and infrared properties of Nix Mn1-xFe_2O_4 ferrites. J. Mater. Sci. **36**, 5115–5118 (2001)
4. E.E. Ateia, M.A. Ateia, M.M. Arman, Under publication. J. Mater. Sci. Mater. Electron. (2021). https://doi.org/10.21203/rs.3.rs-312141/v1
5. J. Hua, Y. Liu, L.W.M. Feng, J. Zhao, H. Li, Mossbauer studies on Mn substituted $CoFe_2O_4$/Sio_2 nanocomposite synthesized by sol-gel method. J. Magn Magn Mater **402**, 166–171 (2016)
6. P.S. Aghav, V.N. Dhage, M.L. Mane, D.R. Shengule, R.G. Dorik, K.M. Jadhav, effect of aluminium substitution on the structural and magnetic properties of cobalt ferrite synthesized by sol-gel auto combustion process. Physica B **406**, 4350–4354 (2011)
7. K. Venkateson, D.R. Babu, M.P.K. Bai, R. Supriya, R. Vidya, S. Medeswaran, P. Anandan, M. Arivanandhan, Y. Hoyakawa, Structural and magnetic properties of cobalt doped iron oxide nanoparticles prepared by solution combustion method for biomedical application. Int. J. Nanomed. **10**(Suppl 1), 189–198 (2015)
8. E.E. Ateia, A.A. El-Bassuony, G. Abdelatif, F.S. Soliman, J. Mater. Sci. Mater. Electron. **28**, 241–249 (2017)
9. E.E. Ateia, R. Ramadan, A.S. Shafaay, Appl. Phys. A **126**, 222 (2020)
10. S.M. Hosseinpour-Mashkani, M. Maddahfar, A. Sobhani-Nasab, Precipitation, synthesis, characterization, morphological, control and photo catalyst application of $ZnWO_4$. J. Electron Mater. **45**, 3612 (2016)
11. D. Erdem, N.S. Bingham, F.J. Heiligtag, N. Pilet, P. Warinicke, L.J. Heyderman, M. Niederberger, $CoFe_2O_4$ and $CoFe_2O_4$-SiO_2 nanoparticle thin films with perpendicular magnetic anisotropy for magnetic and magneto-optical applications. Adv. Funct. Mater. **26**(12), 1954–1963 (2016)
12. Z. Huai-Wu, L. Jie, S. Hua, Z. Ting-Chuan, L. Yang, Z.Z. Liang, Development and application of ferrite materials for law temperature–Co–fired ceramic technology. Chin. Phys. B **22**(11), 117504 (2013)
13. R.K. Kotnala, J. Shah, *Handbook of Magnetic Materials* (Elsevier, 2015), pp. 291–379
14. P.N. Anantharamaiah, P.A. Joy, Mater. Sci. **50**, 6510 (2015)
15. B.K. Kuanar, S.R. Mishra, L. Wang, D. Delconte, D. Neupane, V. Veerakumar, Z. Celinski, Mat. Res. Bull. **76**, 22 (2016)
16. I.C. Nlbdim, N. Ranvah, Y. Melikhuve, P.I. Williams, J.E. Snyder, A.-J. Moses, D.C. Jiles, J. Appl. Phys. **107**, 09A936 (2010)
17. L. Kumar, M. Kar, J. Magn. Magn. Mater. **323**, 2042 (2011)
18. E.E. Ateia, F.S. Soliman, Appl. Phys. A **123**, 312 (2017)
19. F. Muthafar, A.L. Hilli, S. Li, S. Kassim, Mater. Chem. Phys. **128**, 127–132 (2011)
20. K. Ramakrishna, K.V. Kumar, C. Ravinderguptha, D. Rvinder, Adv. Mater. Phys. Chem. **2**, 149–154 (2012)
21. D.R. Mane, U.N. Devatwal, K.M. Jadhav, Mater. Lett. **44**, 91 (2000)
22. N. Hanh, O.K. Quy, N.P. Thuy, L.D. Tung, L. Spinu, Phys. B **327**, 382 (2003)
23. S. Singhal, R. Sharma, T. Namgyal, S. Jauhar, S. Bhukal, J. Kaur, Ceram. Int. **38**, 2773 (2012)
24. R.D. Shannon, Acta Cryst. A **32**, 751 (1976)
25. C.C. Wu, S. Kumarakrishan, T.O. Mosan, J. Solid State Chem. **37**, 144 (1981)
26. Q. Lin, Z. Guo, F. Yang, Effect of Al^{+3} substitution on structural and magnetic behavior of $CoFe_2O_4$ ferrite nanomaterials. Nanomaterias (Basel) **8**(10), 750 (2018)
27. N.M. Deraz, A. Alarifi, Processing and evaluation of alumina doped nickel ferrite nanoparticle. Int. J. Electrochem. Sci. **7**, 4585–4595 (2012)
28. M. Khalid, A.D. Chandio et al., Aluminum substitution in Ni-Co based spinel ferrite nanoparticles by sol-gel auto combustion method. J. Elec. Mater. **50**(6), 3302–3311 (2021)
29. S.U. Bhasker, M.R. Reddy, Effect of chromium substitution on structural, magnetic, and electrical properties of magneto-ceramic cobalt ferrite nano-particles. J. Sol-Gel. Sci. Technol. **73**(2), 396–402 (2015)
30. S.N. Kane, M. Satalkar, Correlation between magnetic properties and cationic distribution of $Zn_{0.85}$−xNix$Mg_{0.05}Cu_{0.1}Fe_2O_4$ nanospinel ferrite: effect of Ni doping. J. Mater. Sci. **52**(6), 3467–3477 (2017)
31. K.E. Sickafus, J.M. Wills, N.W. Grimes, Structure of spinel. J. Am. Ceram. Soc. **82**, 3279–3292 (1999)
32. E.E. Ateia, M.K. Abdelmaksoud, H. Ismail, J. Mater. Sci. Mater. Electron. **32**, 4480–4492 (2021)
33. R.S. Alam, M. Moradi, M. Rostami, H. Nikmanesh, R. Moayedi, Y. Bai, Structural, magnetic and microwave absorption properties doped Ba-hexaferrite nanoparticles synthesized by coprecipitation method. J. Magn. Magn. Mater. **381**, 1–9 (2015)
34. Q. Lin, Y. He, Xu. Jianmei, J. Lin, Z. Guo, F. Yaung, Effect of Al^{+3} substitution on structural and magnetic behavior of $CoFe_2O_4$ ferrite nanomaterials. Nanomaterials **8**, 750 (2018)
35. S. Gowreesan, A.R. Kumar, Effect of Mg^{2+} ion substitution on structural and electric studies of spinel structure of

$Co_{1-x}Mg_xFe_2O_4$. J. Mater. Sci. Mater. Electron. **28**(6), 4553–4564 (2017)
36. M. Lkshmi, K.V. Kumar, K. Thyagarajan, Structural and magnetic properties of Cr-Co nano ferrite particles. Adv. Nanopart. **5**(1), 103–113 (2016)
37. E.E. Ateia, A.T. Mohamed, M. Morsy, Chapter 5 in Metal Oxide-Carbon Hybrid Materials. Elsevier, Included in the series entitled METAL OXIDES Under publication 2021
38. A. Yaseen, T.H. Mubarak, S.M.A. Ridha, An effect of calcination temperatures on the charecteristics of the $MgFe_2O_4$ nanoferrite prepared using auto combustion method. J. Bio. Chem. Tech. **4**, 9–14 (2018)
39. M.A. Gabal, A.M. Abdel-Daiem, Y.M.A. Angari, I.M. Ismail, Influence of Al substitution on structural, electrical and magnetic properties of Mn-Zn ferrites nano powder prepared via the sol-gel auto-combustion method. Polyhedron **57**, 105–111 (2013)
40. E.E. Ateia, M. Farag, Synthesis of cobalt/calcium nanoferrites with controllable physical properties. Appl. Phys. A **125**, 324 (2019)
41. M.A. Almessiere, Y. Slimani, A. Baykal, Ceram. Int. **44**, 9000 (2018)
42. C. Singh, E.E. Ateia, S.B. Naarang, M. Farag, J. Singh, D.E.E. Nashar, Ceram. Int.**47**(5), 7285–7290 (2021)
43. E.C. Stoner, E.P. Wohlforth, Philos. Trans. R Soc. Land. A **240**(826), 599–642 (1948)
44. Q. Li, C.W. Kartikowati, S. Horie, T. Ogi, T. Iwaki, K. Okuyama, Correlation between particle size/domain structure and magnetic properties of highly crystalline Fe_3O_4 nanoparticles. Sci. Rep. **7**, 9894 (2017)
45. A.T. Raghavender, R.G. Kulkarni, K.M. Jadhav, Magnetic properties of mixed cobalt aluminum ferrite nanoparticles. Chin. J. Phys. **48**(4), 512–522 (2010)
46. H.M. Zaki, S.H. Al-Heniti, A. Hashhash, Effect of Al^{3+} ion addition on the magnetic properties of cobalt ferrite at moderate and low temperatures. J. Magn. Magn. Mater. **401**, 1027–1032 (2016)
47. Y. Yafet, C. Kittel, Antiferromagnetic arrangements in ferrites. Phys. Rev. **87**, 290–294 (1952)
48. R. Topkaya, A. Baykal, A. Demir, Yafet-Kittel-type magnetic order in Zn-substituted cobalt ferrite nanoparticls with uniaxial anisotropy. J. Nanopart. Res. **15**, 1359 (2013)
49. N.S.S. Murthy, M.G. Natera, S.I. Youssef, R.J. Begum, C.M. Srivastava, Yafet-Kittel angles in zinc-nickel ferrite. Phys. Rev. **181**(2), 969–977 (1969)
50. E.E. Ateia, A.T. Mohamed, K. Elsayed, J. Magn. Magn. Mater. **452**, 169–178 (2018)
51. M. Ajmal, A. Maqsood, Structural, electrical and magnetic properties of Cu1-xZnxFe_2O_4 ferrite ($0 \leq x \leq 1$). J. Alloys Compd. **460**(1–2), 54–59 (2008)
52. S.A. Mazen, N.I. Abu-Elsaad, Structural and some magnetic properties of manganese-substituted lithium ferrites. J. Magn. Magn. Mater. **324**(20), 3366–3373 (2012)
53. S. Raghuvanshi, F. Mazaleyrat, S.N. Kane, $Mg_{1-x}Zn_xFe_2O_4$ nanoparticles: interplay between cation distribution and magnetic properties. AIP Adv. **8**, 047804 (2018)
54. T.R. Tatarchuk, M. Bououdina, N.D. Paliychuk, Structural characterization and antistructure modeling of cobalt-substituted zinc ferrites. J. Alloys Compd. **694**(15), 777–791 (2016). https://doi.org/10.1016/j.jallcom.10.067
55. K.V. Zipare, S.S. Bandgar, G.S. Shahane, Effect of Dy-substitution on structural and magnetic properties of Mn-Zn ferrite nanoparticles. J. Rare Earths **36**(1), 86–94 (2017)
56. T. Hauet, L. Piraux, S.K. Srivastava, V.A. Antohe, D. Lacour, M. Hehn, F. Montaigne, J. Schwenk, M.A. Marioni, H.J. Hug, Phys. Rev. B **89**, 174421 (2014)